
This is an electronic reprint of the original article.
This reprint may differ from the original in pagination and typographic detail.

Dimmock, A. P.; Osmane, A.; Pulkkinen, T. I.; Nykyri, K.; Kilpua, E.K.J.

Temperature variations in the dayside magnetosheath and their dependence on ion-scale magnetic structures

Published in:
Journal of Geophysical Research: Space Physics

DOI:
[10.1002/2016JA023729](https://doi.org/10.1002/2016JA023729)

Published: 01/06/2017

Document Version
Publisher's PDF, also known as Version of record

Please cite the original version:
Dimmock, A. P., Osmane, A., Pulkkinen, T. I., Nykyri, K., & Kilpua, E. K. J. (2017). Temperature variations in the dayside magnetosheath and their dependence on ion-scale magnetic structures: THEMIS statistics and measurements by MMS. *Journal of Geophysical Research: Space Physics*, 122(6), 6165-6184.
<https://doi.org/10.1002/2016JA023729>

This material is protected by copyright and other intellectual property rights, and duplication or sale of all or part of any of the repository collections is not permitted, except that material may be duplicated by you for your research use or educational purposes in electronic or print form. You must obtain permission for any other use. Electronic or print copies may not be offered, whether for sale or otherwise to anyone who is not an authorised user.

RESEARCH ARTICLE

10.1002/2016JA023729

Key Points:

- A positive correlation exists between the amplitude of magnetic fluctuations and temperature variation
- Temperature fluctuations are strongly associated with larger local ion-scale magnetic structures than the fluid input at the shock
- The amplitude of ion gyroscale fluctuations and in situ temperature variations are favored by the dawn flank

Correspondence to:

A. P. Dimmock,
andrew.dimmock@aalto.fi

Citation:

Dimmock, A. P., A. Osmane, T. I. Pulkkinen, K. Nykyri, and E. Kilpua (2017), Temperature variations in the dayside magnetosheath and their dependence on ion-scale magnetic structures: THEMIS statistics and measurements by MMS, *J. Geophys. Res. Space Physics*, 122, 6165–6184, doi:10.1002/2016JA023729.

Received 25 NOV 2016

Accepted 26 MAY 2017

Accepted article online 30 MAY 2017

Published online 14 JUN 2017

Temperature variations in the dayside magnetosheath and their dependence on ion-scale magnetic structures: THEMIS statistics and measurements by MMS

A. P. Dimmock¹ , A. Osmane¹ , T. I. Pulkkinen¹ , K. Nykyri² , and E. Kilpua³

¹Department of Electronics and Nanoengineering, School of Electrical Engineering, Aalto University, Espoo, Finland,

²Centre for Space and Atmospheric Research, Embry-Riddle Aeronautical University, Daytona Beach, Florida, USA,

³Department of Physics, University of Helsinki, Helsinki, Finland

Abstract The magnetosheath contains an array of waves, instabilities, and nonlinear magnetic structures which modify global plasma properties by means of various wave-particle interactions. The present work demonstrates that ion-scale magnetic field structures ($\sim 0.2\text{--}0.5$ Hz) observed in the dayside magnetosheath are statistically correlated to ion temperature changes on orders 10–20% of the background value. In addition, our statistical analysis implies that larger temperature changes are in equipartition to larger amplitude magnetic structures. This effect was more pronounced behind the quasi-parallel bow shock and during faster solar wind speeds. The study of two separate intervals suggests that this effect can result from both local and external drivers. This manuscript presents two separate case studies, one from using THEMIS (Time History of Events and Macroscale Interactions during Substorms) data and another from Magnetospheric Multiscale; these measurements are then supported by extensive THEMIS statistical observations. These results could partly explain the 10–20% dawn-favored asymmetry of the magnetosheath ion temperature seed population and contribute to the dawn-favored asymmetry of cold component ions in the cold dense plasma sheet.

1. Introduction

The interaction between the supermagnetosonic solar wind and the Earth's dipole magnetic field generates a fast mode collisionless shock wave that stands approximately 15 Earth radii (R_E) upstream of the planet. The plasma, which has been processed by the bow shock, is housed in the magnetosheath; it is hotter, slower, denser, and magnetically reconfigured compared to its upstream counterpart. The magnetosheath extends Earthward until the magnetopause, which is the boundary that marks the balance between the magnetospheric and solar wind pressures. More importantly, the magnetopause is where the majority of solar wind plasma gains entry to the inner magnetosphere via numerous transport mechanisms. In other words, the state of the magnetosheath regulates plasma entry into the magnetosphere, and as a result, its global and local plasma dynamics are therefore fundamental to solar wind-magnetosphere coupling. However, the magnetosheath state is far from straightforward since it is a nonlinear collection of waves, instabilities, and turbulence, which are delicately coupled to regularly changing upstream conditions.

The magnetic configuration of the magnetosheath [see *Fairfield*, 1976] and profile of the plasma flow are responsible for the two dominant plasma transport processes: magnetic reconnection [*Dungey*, 1961] and the Kelvin-Helmholtz Instability (KHI) [*Miura and Pritchett*, 1982]. The former is initiated around the subsolar magnetosheath during southward orientated Interplanetary Magnetic Field (IMF) [*Dungey*, 1961] when the adjacent field lines are antiparallel. The reconnection rate is impacted by the local magnetosheath properties such as magnetic field strength, direction, and plasma density [*Borovsky et al.*, 2008], but open questions remain on the specific role of local magnetosheath conditions regulating reconnection rates. On the other hand, KHI grows from the velocity shear experienced by plasma adjacent to the magnetopause and provides plasma transport during its nonlinear stage; mainly through reconnection in its “rolled up” vortex structure [*Nykyri and Otto*, 2001]. This process is also dependent on the local plasma parameters, namely, the tangential (to k) magnetic field strength and flow velocity. To add complexity, the magnetosheath is asymmetric by nature, and during a Parker-spiral IMF, magnetic field strength, flow velocity, and temperature anisotropy (T_{\perp}/T_{\parallel}) favor the dusk quasi-perpendicular (Q_{\perp}) flank whereas ion density and temperature favor the dawn

quasi-parallel (Q_{\parallel}) side [Paularena et al., 2001; Němeček et al., 2003; Longmore et al., 2005; Walsh et al., 2012; Lavraud et al., 2013; Dimmock and Nykyri, 2013]. However, the picture is even more complicated as the magnetosheath is home to abundant local multiscale waves and instabilities. These transient properties may be responsible for driving some dawn-dusk asymmetries such as ion temperature [Dimmock et al., 2015] but may also affect the reconnection rate and the plasma transport associated with KHI.

Mirror mode waves [Hasegawa, 1969] dominate the magnetosheath turbulence spectra in the range of 10–20 s [Soucek et al., 2008; Dimmock et al., 2015]. They grow from the free energy provided by $T_{\perp}/T_{\parallel} > 1$, which is introduced at the bow shock transition where perpendicular nonadiabatic heating [Lee et al., 1986, 1987] is greater than the more adiabatically heated parallel temperatures [Biskamp and Welter, 1972]. Competing with mirror modes is the ion cyclotron instability [Gary et al., 1993]; however, these are favored by lower plasma β conditions and therefore statistically mirror modes are globally more dominant. Anisotropy instabilities such as these are inherently linked to both adiabatic temperature changes (such as that around the magnetopause) and nonadiabatic heating (e.g., through waves and instabilities) [Chaston et al., 2013]. As a result, there is a complex nonlinear dependency (e.g., nonlinear cascading) between these multiscale processes, which regulate the background plasma.

At higher frequencies, specifically those close to the ion cyclotron frequency, the situation is different. Numerous studies [Fairfield, 1976; Luhmann, 1986; Shevyrev et al., 2007; Yao et al., 2011; Walsh et al., 2012; Chaston et al., 2013; Dimmock et al., 2014, 2015] all agree that the amplitude of ion-scale magnetic field turbulence is greater on the dawn magnetosheath as opposed to the mirror-mode-favored duskside. The origin of dawnside turbulence can be attributed to at least several processes. Examples of these include the following: Q_{\parallel} bow shock dynamics [Thomas et al., 1990; Winske et al., 1990], foreshock processes [Eastwood et al., 2002; Blanco-Cano et al., 2006; Gutynska et al., 2015], ambient solar wind fluctuations [Engebretson et al., 1991], and other locally generated waves and instabilities such as Kinetic Alfvén Waves (KAW). Through nonlinear wave-particle interactions, these transient processes can significantly modify the local plasma conditions to such an extent that global conditions are affected. With abundant multispacecraft measurements such as Cluster, Time History of Events and Macroscale Interactions during Substorms (THEMIS), and Magnetospheric Multiscale (MMS), and the increasing sophistication of numerical simulations, it is becoming increasingly apparent that kinetic effects in the magnetosheath can have global effects (e.g., on plasma transport). Therefore, it is fundamentally important to quantify the kinetic properties in the magnetosheath to build a complete description.

An example of wave-particle interactions that has attracted deserved attention is that of nonadiabatic ion heating by KAWs. This was theoretically studied by Johnson and Cheng [2001] in the form of stochastic ion heating close to the magnetopause. The authors suggested that if wave amplitudes are sufficiently large ($\delta B_{\perp}/B_0 > 0.05$), stochastic particle orbits could deplete the ion distribution core, causing them to migrate to higher energies. This widens the particle distribution and is indicative of an increase in the ion kinetic temperature.

The above work was further strengthened by Chaston et al. [2008], who (using THEMIS measurements) showed that broadband electromagnetic waves at the magnetopause caused heating and plasma transport. The turbulence spectra they studied were consistent with KAWs or those that underwent Doppler shift. The wave-particle interaction from KAW resulted in particle acceleration, which was recorded as parallel and perpendicular ion heating. What is noteworthy is that if amplitudes are sufficiently large, they can produce diffusive plasma transport.

A similar conclusion was reached by Yao et al. [2011] also using THEMIS data. The authors reported that ion gyroscale magnetic field perturbations were larger on the dawnside adjacent to the magnetopause. These variations could heat ions and therefore facilitate additional plasma transport through diffusive means. Johnson and Wing [2009] suggested that changes in entropy can be indicative of nonadiabatic heating processes near the magnetopause for different plasma populations.

KAWs at the magnetopause could be generated by mode conversion from the convection of compressional waves. This physical scenario was proposed by Johnson and Cheng [1997] who stated that quasi-linear theory suggests KAWs can drive plasma transport in which diffusion coefficients and convection speeds of $D_{\perp} \sim 10^9$ m²/s and 1 km/s, respectively.

This effect is not constrained to the magnetopause. *Chaston et al.* [2013] has shown that nonadiabatic heating takes place not only at and around the magnetopause but also across the magnetosheath in general. The authors studied adiabatic invariants as a function of the power spectral density (PSD) of magnetic field structures close to the ion gyrofrequency. They noticed that larger PSD values resulted in an increase of the adiabatic invariants which were consistent with the previous experimental and theoretical works by *Johnson and Cheng* [1997, 2001] and *Yao et al.* [2011]. Based on their calculations of parallel and perpendicular heating rates, they concluded that KAWs were more efficient in generating perpendicular heating. By affecting the local temperature anisotropy, this process provides a potential link between ion-scale waves and larger scale anisotropic instabilities such as mirror modes.

Recently, *Moore et al.* [2016] showed in situ observations of ion heating by fast magnetosonic wave modes during a nonlinear KH vortex. This cross-scale energy transport could also be a fundamental heating mechanism which could be crucial in understanding the coupling between fluid and ion-scale mechanisms in the magnetosheath.

It is also worth mentioning that alternative kinetic heating mechanisms are present on the dawn flank, which are not driven by electromagnetic waves. Recently, in a synergetic study using experimental and theoretical data, *Karimabadi et al.* [2014] suggested a link between reconnecting current sheets [*Retinò et al.*, 2007] and the turbulence induced by the Q_{\parallel} shock. This process acts as a heating source, which is not present (to our knowledge), or statistically less frequent, on the duskside [*Karimabadi et al.*, 2014]. This mechanism could be fundamental to raising ion temperatures on the dawnside above those on the dusk flank. It is plausible that this could be a contributing factor to the magnetosheath dawn-favored ion temperature asymmetry observed in experimental data.

Kinetic properties in the magnetosheath are not decoupled from the global background properties, and their effects are measurable. Dawnside magnetosheath heating via magnetic reconnection [*Karimabadi et al.*, 2014], broadband electromagnetic waves [*Chaston et al.*, 2013], and other magnetic structures may explain the dawn-favored ion temperature asymmetry observed in experimental data [*Walsh et al.*, 2012; *Dimmock et al.*, 2015]. In addition to these, wave-particle interactions close to the magnetopause [*Johnson and Cheng*, 2001; *Chaston et al.*, 2008; *Yao et al.*, 2011] may account for the difference in the 10–20% magnetosheath asymmetry and the 40% dawn-favored asymmetry in the cold dense plasma sheet [*Wing et al.*, 2005]. The motivation of the present study is to expand on our previous work regarding dawn-dusk asymmetries of magnetosheath ion temperature [*Dimmock et al.*, 2015] and ion-scale magnetic field fluctuations [*Dimmock et al.*, 2014] to quantify the statistical dependency between these two quantities. We place no preference on any specific mechanism and focus entirely on the relationship between the amplitude of magnetic fluctuations and the local changes in ion temperature. The work here is also an extension of previous studies [*Chaston et al.*, 2008; *Yao et al.*, 2011; *Chaston et al.*, 2013] but differs significantly on many aspects. First, we measure directly the relative temperature changes (with respect to ambient value) during enhanced ion-scale field variations and study their statistical relationship with the amplitude of magnetic structures. Second, we quantify the dawn-dusk asymmetry and investigate the role of the solar wind speed as an external driver. Finally, our analysis differs to that of previous studies by examining the Probability Distribution Functions (PDFs) of the temperature changes for local and external drivers based on extensive (72,000) statistical observations over an 8 year period. The statistical data are complimented by two case studies (from THEMIS and MMS) suggesting that the nature of in situ temperature changes can originate locally or externally. The THEMIS case study is more consistent with external driving (manifesting as localized heating) by atypical upstream conditions in the form of IMF rotations and discontinuities. The MMS event is more consistent with local heating produced by electromagnetic plasma waves.

The manuscript will be structured as follows. Section 2 will describe the data sets and instrumentation required to complete this study. Section 3 will provide a detailed description of how these data are processed involving as follows: (a) magnetosheath data coordinate transformation, (b) magnetic field spectral analysis, (c) estimation of relative ion temperature changes, and (d) determining the statistical correlation between (b) and (c). We will present two case studies and our statistical observations in section 4, before discussing their physical interpretation and implications in section 5. We will draw our conclusions and provide a summary in section 6.

2. Data Sets

We used THEMIS [Angelopoulos, 2008] measurements between October 2007 and December 2015 to construct a statistical database of dayside magnetosheath observations. Magnetic field observations were obtained via the FluxGate Magnetometer (FGM) instrument [Auster et al., 2008] on-board each probe in which we used the 4 Hz low-resolution “FGL” data product. Ion temperature measurements were provided by the level 2 spin resolution (~ 3 s) moments provided by the ElectroStatic Analyzer instrument [McFadden et al., 2008]. For estimates of solar wind parameters, the 1 min OMNI database was used over the corresponding THEMIS interval. At the time of this study, OMNI data had been compiled from the ACE and Wind solar wind measurements near Lagrangian point L1 before being propagated [King and Papitashvili, 2005] to the bow shock nose location. This was estimated using the Farris and Russell [1994] model. All OMNI data were downloaded from the NASA OMNIweb service (<http://omniweb.gsfc.nasa.gov>) and THEMIS data files were obtained through the Berkeley THEMIS web interface at <http://themis.ssl.berkeley.edu/index.shtml>.

We also utilized data from the Magnetospheric MultiScale (MMS) mission [Burch et al., 2016]. Magnetic field time series were recorded by the MMS FGM instrument [Russell et al., 2016], and we used the fast survey data product. For plasma measurements such as velocity, density, and ion temperatures, we used the L2 moments from the Fast Plasma Investigation (FPI) instrument [Pollock et al., 2016]. All MMS data were downloaded through the MMS Science Data Center accessible at <https://lasp.colorado.edu/mms/sdc/public/>. The versions of the data files used were _v4.18.0. and _v2.1.0. for the FGM and FPI data, respectively.

3. Methodology

3.1. Compilation of Dayside Magnetosheath Database

Due to the dynamic behavior of the magnetosheath and its boundary layers, large-scale statistical investigations are troublesome from both technical and physical perspectives. To address this, we utilized our previously developed data analysis tool [Dimmock and Nykyri, 2013] to extract magnetosheath observations from the THEMIS catalog from January 2008 to December 2015. To represent the magnetosheath, we transformed each THEMIS location from the GSE frame, into the Magnetosheath InterPlanetary Medium Reference (MIPM) frame. First, this required the computation of the Geocentric InterPlanetary Medium (GIPM) reference frame in which the x axis (\hat{X}_{gipm}) is aligned with the upstream solar wind flow direction. Typically, the Earth’s orbital speed is removed from the solar wind V_y measurement to adjust for planetary aberration; however, this was already accounted for in the OMNI data. The y axis was computed based on the upstream IMF direction

$$Y_{\text{gipm}}^{\wedge} = \begin{cases} -\vec{B} + \left(\vec{B} \cdot X_{\text{gipm}}^{\wedge} \right) X_{\text{gipm}}^{\wedge} / |\vec{B}| - \left(\vec{B} \cdot X_{\text{gipm}}^{\wedge} \right) X_{\text{gipm}}^{\wedge} / |\vec{B}|, & \text{if } \left(\vec{B} \cdot X_{\text{gipm}}^{\wedge} \right) > 0, \\ +\vec{B} - \left(\vec{B} \cdot X_{\text{gipm}}^{\wedge} \right) X_{\text{gipm}}^{\wedge} / |\vec{B}| - \left(\vec{B} \cdot X_{\text{gipm}}^{\wedge} \right) X_{\text{gipm}}^{\wedge} / |\vec{B}|, & \text{if } \left(\vec{B} \cdot X_{\text{gipm}}^{\wedge} \right) < 0, \end{cases} \quad (1)$$

and \hat{Z}_{gipm} completes the orthogonal set, i.e., $(\hat{X}_{\text{gipm}} \times \hat{Y}_{\text{gipm}})$. The GIPM magnetosheath statistically resembles the configuration during a typical 45° Parker-spiral IMF orientation in such a manner that the dawn and dusk flanks lie downstream of a Q_{\parallel} and Q_{\perp} bow shock, respectively. For example, if an observation were made on the dawn flank during an ortho Parker-spiral IMF, then this point would be relocated to duskside. Therefore, from now on we adopt exclusively Q_{\parallel} and Q_{\perp} to refer to the dawn and dusk flanks, respectively.

To account for the continual motion of the magnetosheath boundaries, at each THEMIS location (\vec{R}), the radial magnetopause (r_{mp}) and bow shock (r_{bs}) locations are determined using the Shue et al. [1998] and Verigin et al. [2006] models, respectively. For each model, the OMNI data acted as a solar wind monitor, providing the model input parameters. In this case (and the GIPM calculation), 20 min averages of each solar wind quantity were used. The 20 min average accounted for the unknown convection time to the magnetosheath measurement and minimized the impact from solar wind transient (few minutes) behavior. To complete the MIPM transformation, each GIPM data point is normalized between the model boundary positions, therefore providing a fractional distance computed from the following expression:

$$F_{\text{mipm}} = \frac{|\vec{R}| - r_{\text{mp}}}{r_{\text{bs}} - r_{\text{mp}}}. \quad (2)$$

The value of F_{mipm} can be used to identify the following regions:

$$F_{\text{mipm}} = \begin{cases} [0 \rightarrow 1] & \text{magnetosheath} \\ < 0 & \text{magnetosphere} \\ > 1 & \text{solar wind} \\ 1 & \text{bow shock} \\ 0 & \text{magnetopause.} \end{cases} \quad (3)$$

The MIPM coordinates are described by the fractional distance (F_{mipm}), zenith (θ_{mipm}), and clock (ϕ_{mipm}) angles. These angles are defined as follows: $\theta_{\text{mipm}} = \arccos((\vec{R} \cdot \hat{X}_{\text{gipm}})/R)$ and $\phi_{\text{mipm}} = \arctan((\vec{R} \cdot \hat{Z}_{\text{gipm}})/(\vec{R} \cdot \hat{Y}_{\text{gipm}}))$. Advantages for using the MIPM frame are the following: (1) correction for boundary motion, planetary aberration, and IMF rotation, (2) analysis of long-term magnetosheath data sets, and (3) capability to highlight asymmetries and features associated with Q_{\parallel} and Q_{\perp} shock regimes. For equatorial statistical maps presented later (Figures 4 and 5), we collapse points based on $|\phi| \leq 30^{\circ}$. However, for the main statistical analysis (Figures 6–9), this step is not necessary since these results are applicable to the dayside magnetosheath—i.e., they are not restricted to a specific plane. We should mention that to be thorough, we did reproduce the main statistical results with this same ϕ restriction; the conclusions were unaffected.

An alternative description of this transformation can be found in *Verigin et al.* [2006]. We also direct readers to *Shue et al.* [1998] for details on the computation of r_{mp} . The bow shock model and the parameters used to determine r_{bs} were described in *Verigin et al.* [2001, 2003]. In addition, the complete methodology was described in *Dimmock and Nykyri* [2013].

3.2. Preliminary Data Processing

3.2.1. Processing of Magnetic Field Measurements

The analysis of THEMIS data was performed using 3 min windows centered at each probe location. First, magnetic field data were rotated into a mean (3 min) field-aligned coordinate system $B(\parallel, \perp_1, \perp_2)$ calculated using the GSE magnetic field (\vec{B}) and spacecraft position (\vec{R}) vectors as follows:

$$\hat{B}_{\parallel} = [\langle B_x \rangle, \langle B_y \rangle, \langle B_z \rangle] / \sqrt{\langle B_x \rangle^2 + \langle B_y \rangle^2 + \langle B_z \rangle^2} \quad (4)$$

$$\hat{B}_{\perp 1} = \hat{B}_{\parallel} \times \hat{R} \quad (5)$$

$$\hat{B}_{\perp 2} = \hat{B}_{\parallel} \times \hat{B}_{\perp 1}. \quad (6)$$

Note that all averages (i.e., to estimate \hat{B}_{\parallel}) were computed over the entire 3 min interval. We then compute the magnitudes

$$B_{\parallel} = |\vec{B} \cdot \hat{B}_{\parallel}| \quad (7)$$

$$B_{\perp} = \sqrt{(\vec{B} \cdot \hat{B}_{\perp 1})^2 + (\vec{B} \cdot \hat{B}_{\perp 2})^2}, \quad (8)$$

which were used as a measure of the parallel and perpendicular magnetic field components.

To determine the spectral content of B_{\perp} and B_{\parallel} , we compute the wavelet (B_w) over each 3 min window using a wavelet transform with a Morlet mother wavelet function. In practice, we computed the wavelet coefficients for 10 equally spaced frequencies between $\pm 25\%$ of the ion gyrofrequency (f_{ci}). The final estimate was the mean wavelet, $\langle B_w \rangle$, over those 10 frequencies. From this point, this is designated B_v and is a measure of the ion gyroscale spectra over each 3 min window in nT/\sqrt{s} .

3.2.2. Processing of Ion Temperatures

The motivation of the present study is to investigate the statistical dependence between ion-scale magnetic structures and in situ temperature changes. Here we describe the processing of the L2 onboard ion temperature moments to quantify this. First, consistent with the previous text, we assess the in situ magnetosheath conditions within a 3 min window. For each 3 min window, we separate the ion temperature into two spectral components above (T_H) and below (T_L) 60 s using a high-pass and low-pass filter, respectively. Please note that 60 s refers to a filter cutoff frequency and not a window length and that the original measurement could be reconstructed by the sum of its spectral components, i.e., $T = T_L + T_H$; this was checked to ensure that filter artifacts were not introduced to the data. The scale of 60 s was chosen since it is below the typical ion gyrofrequency (0.2 Hz), and therefore, T_L provides a good measure of the background temperature profile.

Table 1. A List of Subset Conditions and Their Respective Criterion Which Were Used to Compile Our Statistical Data Sets^a

#	Condition	Criterion	Length	Figure
C-01	All data	$B_v > 0.0$	72,037	5 ^b -9
C-02	B_v -1	$B_v > 0.1$	71,869	7, 9
C-03	B_v -2	$B_v > 0.2$	71,846	7, 9
C-04	B_v -3	$B_v > 0.3$	48,933	7, 9
C-05	B_v -4	$B_v > 0.4$	32,593	7, 9
C-06	B_v -5	$B_v > 0.5$	23,255	7-9
C-07	B_v -6	$B_v > 0.6$	17,949	5 ^b , 7, and 9
C-08	Slow solar wind	$ \vec{V}_{sw} < 350$ km/s	20,012	5 ^b , 6, and 8
C-09	Fast solar wind	$ \vec{V}_{sw} > 450$ km/s	20,301	5 ^b , 6, and 8
C-10	Dawn flank	$292.5 < \theta_{mipm} < 337.5$	38,498	5 ^b , 8
C-11	Dusk flank	$22.5 < \theta_{mipm} < 67.5$	33,539	5 ^b , 8
C-12	Northward IMF (NIMF)	$B_z > 0.5 B $	7,231	8
C-13	Southward IMF (SIMF)	$B_z < -0.5 B $	19,729	8
C-14	Parker-spiral IMF (PS-1)	$B_x > (< -)0.25 B $ and $B_y < (>) - 0.25 B $	30,070	8
C-15	Parker-spiral IMF (PS-2)	$B_x > (< -)0.5 B $ and $B_y < (>) - 0.5 B $	9,457	8
C-16	B_v -4 (dawn)	C-05 and C-10	19,737	8
C-17	B_v -4 (dusk)	C-05 and C-11	12,856	8
C-18	Slow (dawn)	C-08 and C-10	9,902	8
C-19	Slow (dusk)	C-08 and C-11	10,110	8
C-20	Fast (dawn)	C-09 and C-10	10,300	8
C-21	Fast (dusk)	C-09 and C-11	10,001	8
C-22	NIMF (dawn)	C-12 and C-10	4,117	8
C-23	NIMF (dusk)	C-12 and C-10	3,114	8
C-24	SIMF (dawn)	C-12 and C-13	10,103	8
C-25	SIMF (dusk)	C-12 and C-13	9,626	8
C-26	PS-1 (dawn)	C-14 and C-10	16,189	8
C-27	PS-1 (dusk)	C-14 and C-11	13,881	8
C-28	PS-2 (dawn)	C-15 and C-10	5,428	8
C-29	PS-2 (dusk)	C-15 and C-11	4,029	8

^aThe size of each data set has also been listed together with the figure in which each criterion is applied.

^bSubset of this database was used in this figure.

Please note that we reproduced the results using a 30 s cutoff, and the important factor here is that the cutoff is sufficiently below the local ion gyrofrequency. The background profile is required for the point-by-point normalization of the temperature. Note, this could be achieved by a mean or median of the 3 min temperature, but in reality, this may not be an accurate measure of the ambient temperature over 3 min. We did not place a narrow limitation on the spectral band for T_H since it cannot reliably be assumed that magnetic field variations at scales within $\pm 25\%$ would generate temperature changes over the exact same range of scales; furthermore, showing a scale-to-scale relationship is not the purpose of this study. In addition, the cumulative effect from multiple ion gyroscale magnetic structures may induce in situ temperature changes over similar, but not exactly the same scale range. To measure the in situ temperature changes, the relative temperature change (T_v) is evaluated which is a function of both T_L and T_H as described below.

$$T_v = 100 \left| \frac{T_H}{T_L} \right|. \quad (9)$$

The units of T_v are %, so it is the relative percentage of T_H with respect to T_L (it is comparable to $\delta T/T$ for scales < 1 min). Please note that T_v is a measure of the absolute value of the temperature changes, and therefore, we do not distinguish between increases (heating) and decreases (cooling) of the temperature.

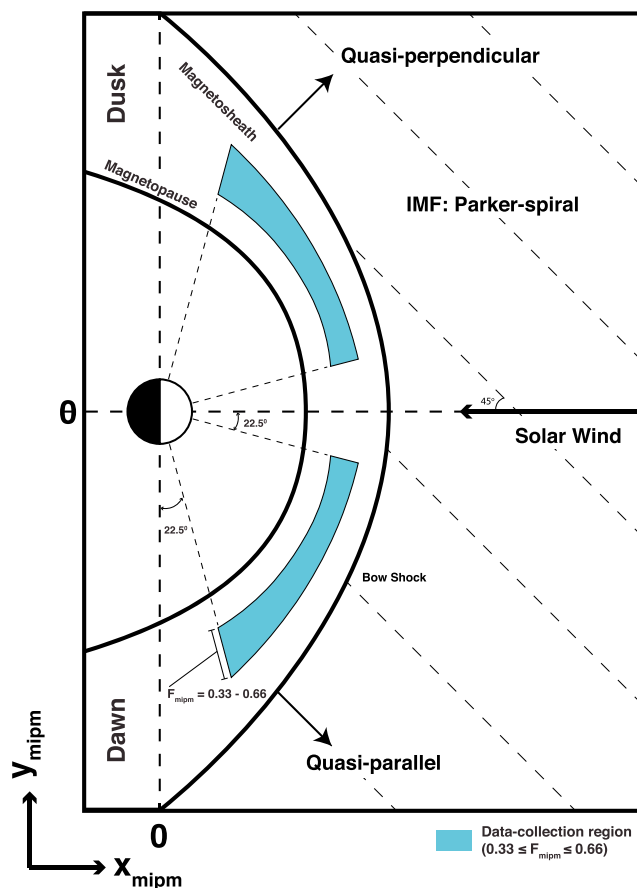


Figure 1. Illustration of the dayside magnetosheath depicting the THEMIS data collection region in the MIPM frame, indicated by the shaded blue region. Please note the following: (1) Not drawn to scale and (2) data collection region in physical space is larger on the dusk flank as it scales with the magnetosheath thickness.

95% yielded the best trade-off with the length of each statistical subset and the associated statistical error. In addition, we excluded all data marked with any quality flags. We explicitly focus on perpendicular components of magnetic field and ion temperature. We did reproduce the following results with the parallel components and achieved the same conclusions. In this case, we do not attempt to distinguish between parallel and perpendicular heating as some effects may be attributed to isotropization of the distribution. To reduce errors associated with boundary inaccuracies, mixed ion temperature distributions, and low data coverage, we imposed constraints on the data collection region of T_v . We only included data in the central magnetosheath ($0.33 < F_{mipm} < 0.66$), thus ignoring data collected close to the magnetosheath boundaries and magnetosheath—magnetosphere mixed plasma populations. An angular sector of 22.5° from θ_{mipm} , meaning our region of analysis is restricted to $22.5 \leq \theta_{mipm} \leq 67.5$. The data collection region is illustrated in Figure 1 by the shaded blue region. This diagram is approximated to the xy plane, but as mentioned earlier, the region extends out of the MIPM xy plane as we impose no limit on ϕ_{mipm} . We can summarize our methodology as follows:

1. GSE to MIPM coordinate transformation (see section 3.1)
2. Isolate data selection region (Figure 1)
3. Calculate FGM wavelet— B_v (section 3.2.1)
4. Compute the relative percentage temperature change— T_v (section 3.2.2 and equation (9))
5. Identify enhanced B_v values and ensure that criteria are met (see Table 1)
6. Interpolate T_v
7. Repeat for all available data

3.2.3. Statistical Data Processing

Since changes in T_v can be less than 3 min, averaging over this time would reduce/remove these effects. Therefore, we identify points in each 3 min window when B_v exceeds a certain threshold. The values of these thresholds are listed in Table 1 and in the individual figures where the data are used. These thresholds were chosen based on the cumulative distribution of B_v and provide an adequate spread across the B_v range while still maintaining good data counts. Within each window, we interpolated (mainly due to the difference in B and T sampling resolution) the value of T_v when each threshold was exceeded. The quantity passed to our statistical data set was the mean of the T_v interpolated values. To ensure that enough points are used, we required that the temporal duration of the total interpolated data reached a minimum of five ion cyclotron wave cycles. For example, if $f_{ci} = 0.2$ Hz, then at least 25 s of data would need to exceed the B_v threshold for those interpolated values to be included in the final data set. To compliment this, we also required 95% data coverage of the magnetic field and ion temperature data within each 3 min window. We did validate every result with 100% coverage; however,

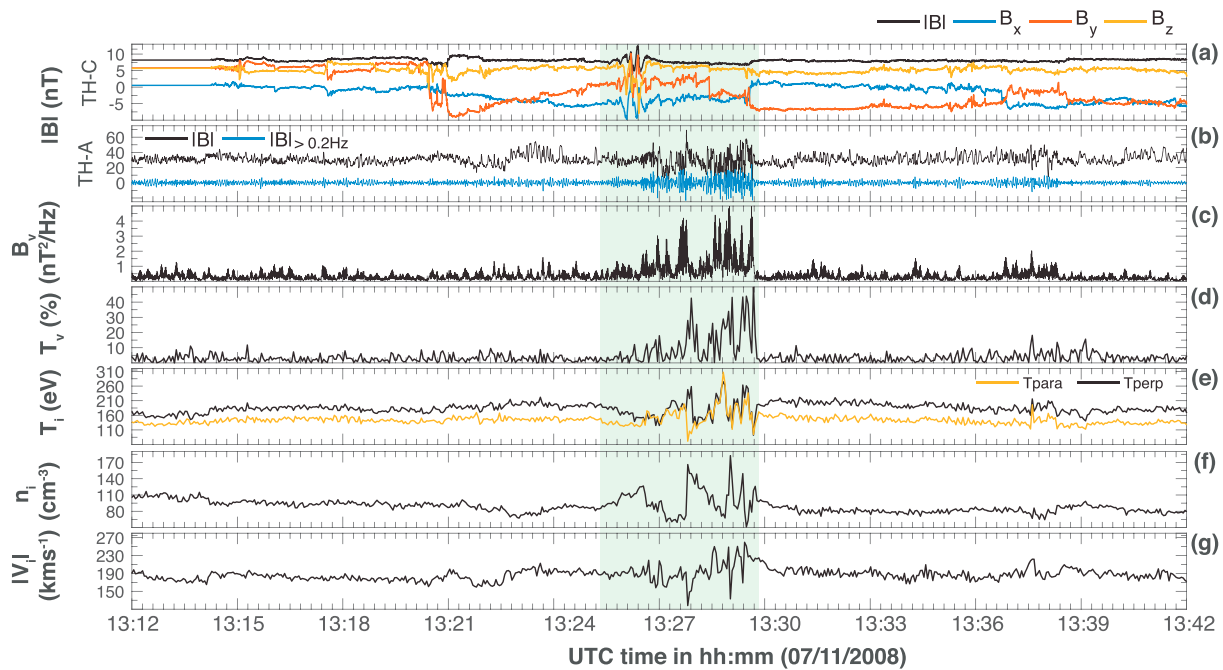


Figure 2. THEMIS time series data recorded on 7 November 2008 between 13:12 and 13:42 UTC. The plot depicts a prolonged solar wind structure recorded by (a) THEMIS-C between 13:21 and 13:30. This corresponds to in situ temperature variations observed by (b–g) THEMIS-A from 13:25 to 13:30. Figures 2a–2g correspond to the following: THEMIS-C magnetic field components, THEMIS-A magnetic field modulus, $|B|$ wavelet, relative temperature change, ion temperatures, ion number density, and flow speed. The green-shaded region indicates the transient structure in the magnetosheath recorded by THEMIS-A.

4. Results

4.1. THEMIS Observations

Shown in Figure 2 are observations recorded by THEMIS-A (TH-A) and THEMIS-C (TH-C) on 7 November 2008 between 13:12 and 13:42 UTC (hh:mm). At this time, the position of TH-A was $R_{a_{gse}} = [5.8, -9.6, -3.15] R_e$ whereas TH-C was located at $R_{c_{gse}} = [7.7, -10.4, -1.0] R_e$. These positions place TH-A on the $Q_{||}$ side magnetosheath and TH-C in the solar wind upstream of the bow shock. By extracting magnetosheath model inputs from the OMNI data, we calculated that the position of TH-A corresponds to a fractional distance of 0.35 at an angle of 302° with respect to the subsolar point. Therefore, the MIPM location is consistent with the $Q_{||}$ flank and is located within the blue-shaded region shown in Figure 1. Figure 2a shows the modulus of the magnetic field recorded by TH-C. The remaining panels show measurements by TH-A. Plotted in Figure 2b are measurements by the TH-A FGM; the back and blue traces correspond to the modulus before and after it has been 0.2 Hz high-pass filtered, respectively. Plotted in Figure 2c is the wavelet of $|B|$ computed in the range of $\pm 25\%$ of the ion gyrofrequency (0.47 Hz). The quantity T_v is plotted in Figure 2d (see equation (9)) which is derived from the perpendicular temperature profile shown in Figure 2e, black trace. Figures 2f and 2g correspond to ion number density and plasma speed, respectively. Between 13:25 and 13:30 (green-shaded region), there is a noticeable enhancement in the amplitude of magnetic field fluctuations around the ion gyrofrequency, as demonstrated clearly by the wavelet in Figure 2c and blue trace in Figure 2a. Interestingly, in concert with the increase of B_v , the ion temperature profile exhibits increased T_v which reach approximately 40%. For convenience, we refer to these events from now on as In situ Temperature Variations (ITVs). The timely occurrence of a large ITV and enhanced B_v is striking, and consistent with statistical observations we present later.

At 13:20, a discontinuity upstream of the bow shock was recorded in which a large rotation of B_y persisted until the end of the ITV ($\sim 13:30$). At 13:26, TH-C observed a transient structure in the solar wind which was around 1 min prior to the ITV in the magnetosheath. This is recognized clearly by the obvious fluctuation of $B_{x,y,z}$. Around 13:26, the local magnetosheath conditions changed, and this marks the beginning of enhancements in B_v . Interestingly, the B_v enhancements cease during the end of the B_y rotation around 13:30. To clarify, the atypical (with respect to preceding conditions) TH-A magnetosheath conditions between 13:26 and 13:30 appear to directly coincide with the start and end of upstream magnetic field rotations seen by TH-C. We attempted to match the measurements from TH-C to foreshock structures but were unsuccessful. In addition,

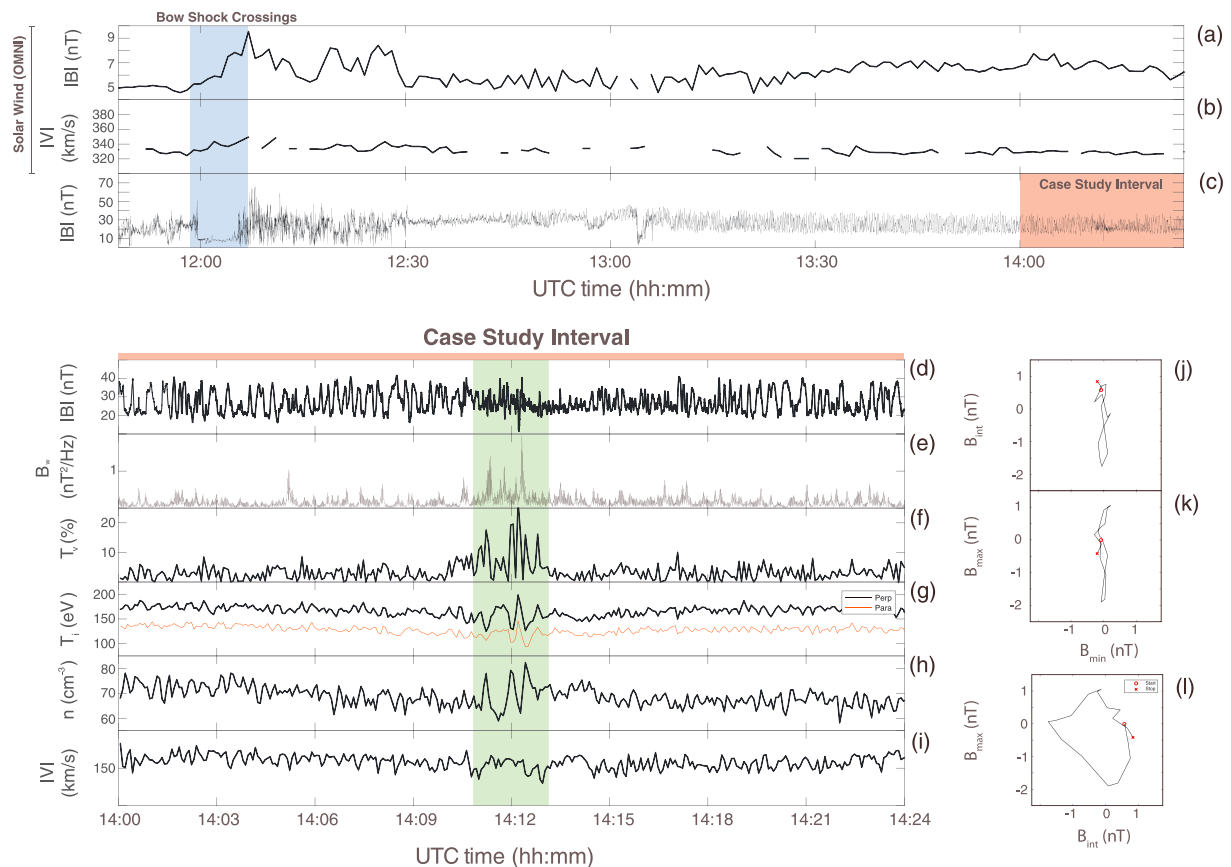


Figure 3. MMS data recorded on 2 November 2015. (a, b) OMNI data of the magnetic field modulus and solar wind speed. (c) An ~2.5 h interval of MMS FGM data showing multiple bow shock crossings (blue-shaded region at 12:00) and then a prolonged period of downstream magnetosheath observations. The red highlighted interval is the area of interest in this study and expanded in the panels below. (d–i) Magnetic field modulus, ion-scale wavelet, magnitude of the relative percentage temperature change, ion temperatures, ion density, and ion velocity. (j–l) Hodograms calculated from data around 14:13:50 using minimum variance analysis. The green region indicated the event and data we analyzed.

TH-C did not appear to observe the foreshock during this interval. Indeed, the timeliness of the TH-C and TH-A observations are striking, and it is not unreasonable to suggest the atypical upstream properties played a strong role.

Although we could not classify this event, the upstream discontinuity and transient features are a remarkable coincidence, and their effects are likely to be observed in the magnetosheath. As a caveat, we should mention that a component (but not all) of the ion moments during this event was flagged as nonzero which suggested possible effects from cold ions. Therefore, by default, it would not be included in our final statistical database; however, comparable events may be included in the statistical data. Nevertheless, this event is a valid and clear demonstration of the statistical relationship we report later. It exhibits how external processes can likely induce in situ effects in the magnetosheath, and due to the rare conditions (e.g., placement of two spacecraft) of its observation, it is worthy of inclusion in this manuscript.

5. MMS Observations

On 2 November 2015 at 11:59:33 UT, the solar wind magnetic field increased from 5 nT to 9.5 nT causing a significant compression of the magnetosphere. As a result, the bow shock location was “pushed back” to approximately 11.8 R_E . This atypically close bow shock meant that the MMS spacecraft could observe the solar wind for around 6 min and measure an inward and outward bow shock traversal. Figures 3a and 3b show the magnetic field strength and solar wind speed extracted from the OMNI data set. Plotted in Figure 3c is the magnetic field modulus from MMS1 clearly showing the two bow shock traversals (~12:00). The enhancement in magnetic field and subsequent bow shock crossings are highlighted in blue across Figures 3a–3c. This case study focused on observations between 14:10:07 UT and 14:14:18 UT and is highlighted in green throughout

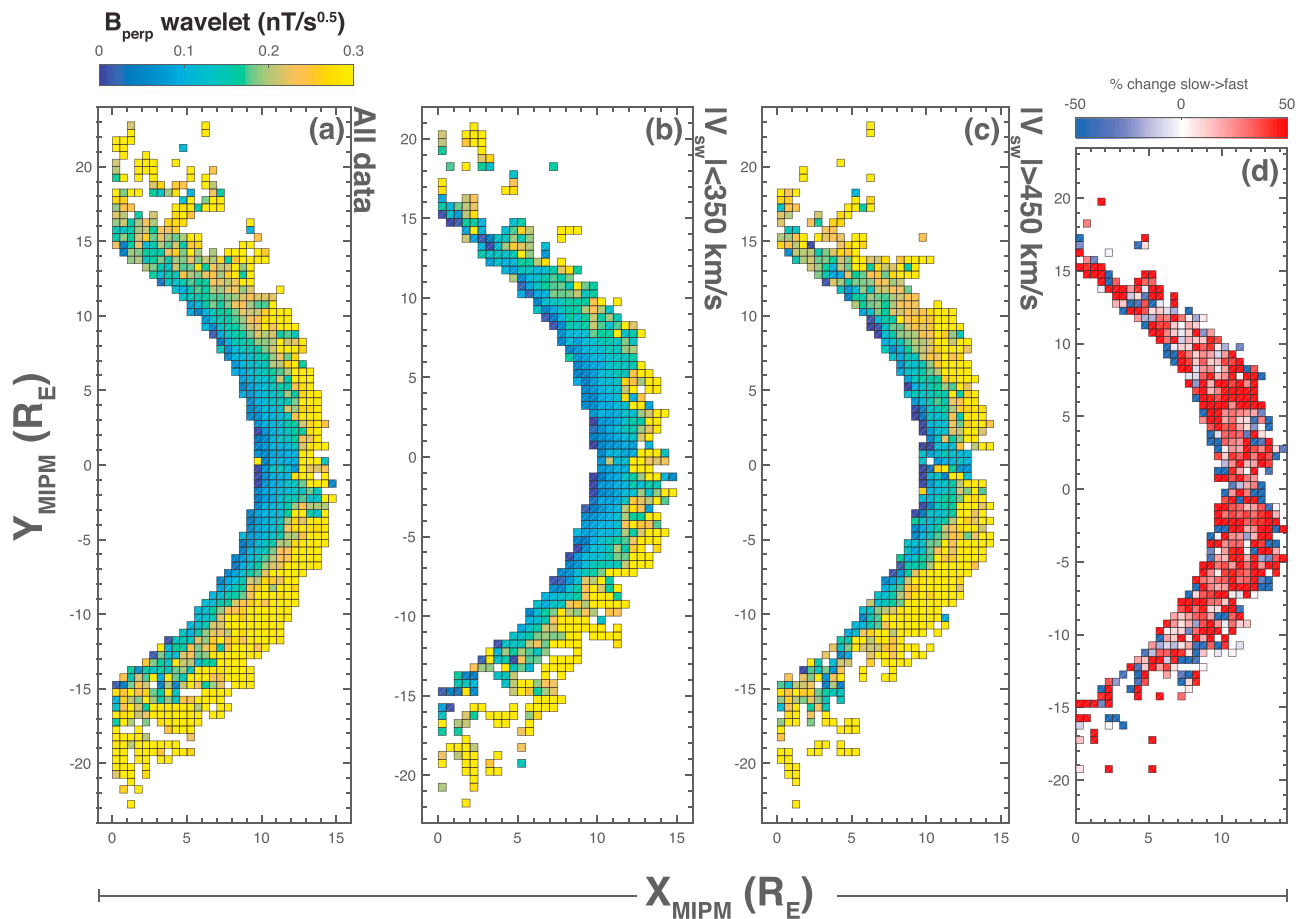


Figure 4. Statistical maps of the mean perpendicular magnetic field wavelet for $\pm 0.25f_{ci}$. (a–c) Data binned for all conditions, $|V_{sw}| < 350$ km/s and $|V_{sw}| > 450$ km/s, respectively. (d) The percentage change between Figures 4b and 4c computed as $100 [(W_{slow} - W_{fast}) / 0.5 (W_{slow} + W_{fast})]$.

Figures 3d–3i. From the OMNI data, we estimate the shock geometry during this interval to be approximately 55° . This is based on the model by *Farris and Russell* [1994], at the upstream location where the spacecraft initially entered the magnetosheath.

The magnetic field measurements in Figure 3d exhibit fluctuations occurring over various time scales, but the majority are around 10–15 s. Around 14:12, there is a noticeable increase in B_v around 0.4–0.5 Hz, which is close to the local ion gyrofrequency. The quantity, B_v , is plotted in Figure 3e. Figures 3f and 3g are T_v (see equation (9)) and the associated temperature profiles. During the region of increased B_v , the value of T_v increased to $\sim 25\%$ from the ambient value of 5%. The simultaneous increase of B_v and T_v are apparent; they appear to coincide directly. What is noteworthy is that the lower frequency (larger scale) variations do not induce any similar comparable response in T_v . In fact, T_v appears to be around or less than 5% before and after the event. The localized variations of temperature are visible in both T_\perp and T_\parallel , but they appear larger in the perpendicular direction. One must err on the side of caution here. The increase in T_\parallel does not indicate parallel heating as isotropization of the distribution can take place [*Chaston et al.*, 2013]; therefore, in this case T_\parallel and T_\perp cannot be decoupled entirely. Figures 3g–3i indicate the temperature profiles, ion number density, and flow speed, respectively. There are also variations in ion number density in concert with the T_v enhancements, but analyses of these are not included in this study.

We performed minimum variance analysis [*Sonnerup and Cahill Jr.*, 1967] to determine the direction of propagation (\hat{k}) and their polarization. From this we obtained a propagation direction of $\hat{k} = (0.82, -0.57, -0.03)$ suggesting directions of $\theta_{kb} = 86.7^\circ$ and $\theta_{kv} = 18.05^\circ$ relative to the background magnetic field and plasma flow directions, respectively. Plotted in Figures 3j–3l are the hodograms over 1 wave cycle. In each hodogram, the red crosses and circles indicate the start and end points of the cycle, respectively. This particular example

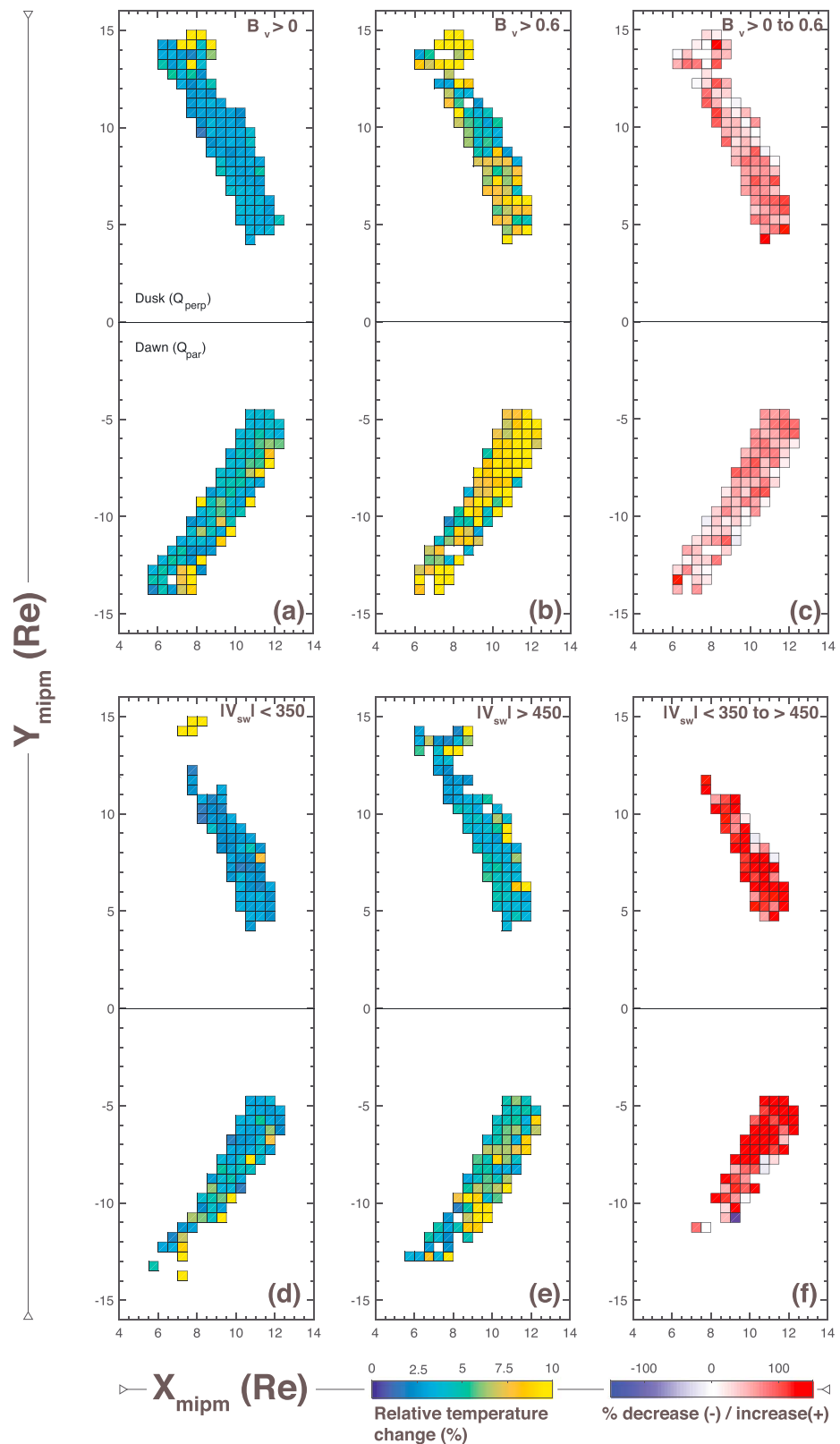


Figure 5. Statistical maps of T_e on the MIPM xy plane. The assigned color represents the median average of point within each bin. The top and bottom rows represent T_e binned as a function of local perpendicular wavelet B_{\perp} , and solar wind speed $|V_{sw}|$, respectively. (c and f) The relative change between panels to the left in each row as percentage points. The bin size is a square 0.5×0.5 Re box. A limit of $|\phi_{mipm}| < 30^\circ$ is enforced to remove points far from XY_{mipm} .

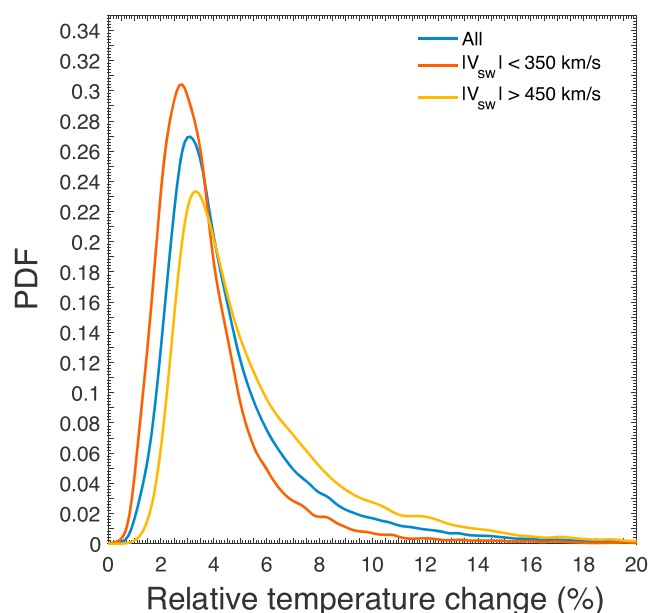


Figure 6. Probability distribution function of T_v for fast (yellow trace) and slow (orange trace) solar wind speeds. The shifting to the right, and the extended tail, implies a larger occurrence of higher amplitude temperature changes during faster solar wind speeds.

solar wind speeds greater than 450 km/s (c). Figure 4d shows the percentage change from slow to fast solar wind speeds computed from $100 \left[\frac{(W_{\text{slow}} - W_{\text{fast}})}{0.5 (WP_{\text{slow}} + WP_{\text{fast}})} \right]$; i.e., it is the percentage change with respect to the average of the corresponding bins. The grid resolution of each square bin is $0.5 \times 0.5 R_e$, and the value assigned to each bin was computed from the median average; this is true for all statistical maps we present in this manuscript. Please note that the data selection region shown in Figure 1 is not applicable here, so the maps contain full dayside coverage. In addition, these data are limited to $|\phi| < 30^\circ$ to restrict points to the MIPM equatorial plane. These data suggest that the largest amplitude variations are close to the bow shock and decrease toward the magnetopause; this effect decreases in concert with tailward distance. What is most noteworthy about these plots is the higher amplitudes present on the Q_{\parallel} flank. In general, the asymmetry $(100 * (\text{dawn} - \text{dusk}) / 0.5 * (\text{dawn} + \text{dusk}))$ is around 35% favored by the Q_{\parallel} flank and can increase by approximately 5 to >10 percentage points during the faster interval. Although this estimate is computed for the region shown in Figure 1 and provides a global quantification, this can vary depending on spatial location. Interestingly, from Figures 1b and 1c, the amplitude of B_v increased for almost all the statistical bins during faster solar wind speeds. In general, the increase of B_v exceeds 50%, but in some bins, it exceeded 100%. Interestingly, there are no significant changes in the spatial distribution of relative increases between the slow and fast subsets, which is evidenced by the uniform increase in Figure 1d. This could be suggestive of similar mechanisms of turbulence that increase in amplitude during higher solar wind speeds.

Plotted in Figure 5 are statistical maps of T_v as a function of solar wind speed and B_v . Please note that the statistical maps have been generated in the region specified in Figure 1. Figures 5a–5c correspond to $B_v > 0$, $B_v > 0.6$, and the relative percentage change. Figures 5d and 5e are the same format as those above but are binned as a function of slow and fast solar wind speeds. The typical value of T_v is between 2% and 5%; however, this is commonly exceeded, as clearly demonstrated in Figures 5d and 5e. In both conditions we tested that T_v increased by over 50%. However, the increase observed as a function of B_v appeared to be greater than that of V_{sw} . Figure 5 also suggests that for both conditions, the value of T_v appears higher on the Q_{\parallel} flank. Although the relative percentage increase is slightly larger for $|V|$, the absolute increase is larger for B_v .

Since the distribution of T_v is non-Gaussian, we plotted the PDF of T_v for fast and slow solar wind speeds in Figure 6. The data corresponding to fast, slow, and all speeds can be identified by the yellow, orange, and blue traces, respectively. The evolution of the PDF from slow to fast conditions is consistent with the statistical maps plotted in Figure 5, confirming an increase of T_v during faster speeds. For the fast solar wind criterion,

indicates that the structures are nearly circularly polarized in the spacecraft frame. The properties discussed above are consistent with a magnetosonic wave mode, or due to the large $(\hat{k} \cdot \vec{V})$ term, could be Doppler-shifted (by plasma flow from small θ_{kv}) KAWs. A similar result of ion heating from Doppler-shifted KAWs was reported by Chaston *et al.* [2013]. We attempted to further this analysis by taking advantage of the multipoint measurements to construct an experimental dispersion relation [Dimmock *et al.*, 2013]. However, the spacecraft separation vectors did not permit the implementation of this technique. Similar analysis was attempted on the THEMIS interval; however, this proved unsuccessful.

5.1. THEMIS Statistical Observations

Presented in Figure 4 are statistical maps of the wavelet vales of the perpendicular magnetic field for all data (a), solar wind speeds less than 350 km/s (b), and

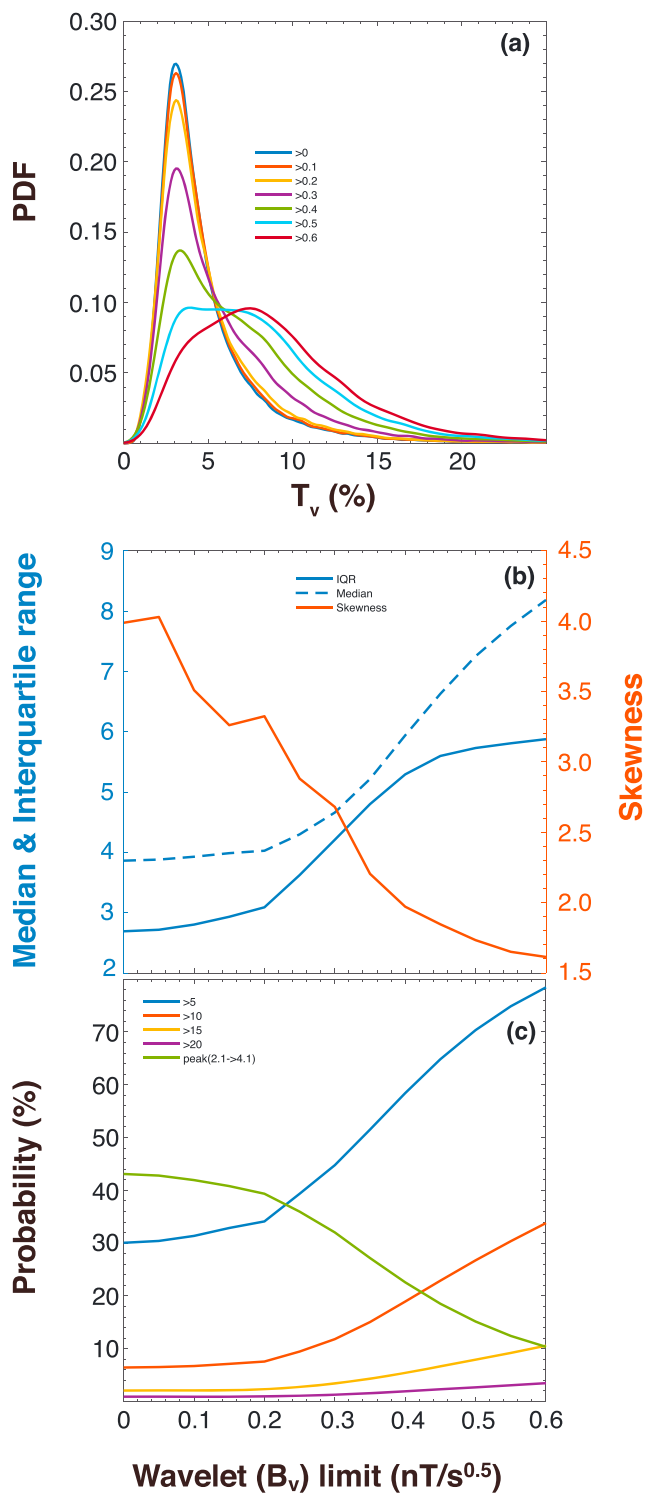


Figure 7. Statistical relationship between ion temperature variations (T_v) and magnetic field perpendicular wavelet (B_w). (a) The PDFs for T_v for varying levels of B_w . (b) The median, interquartile range, and skewness of each distribution plotted in Figure 7a. (c) The line plots correspond to integrals of the PDFs in Figure 7a; they represent the probability of T_v falling within a certain range as a function of B_w .

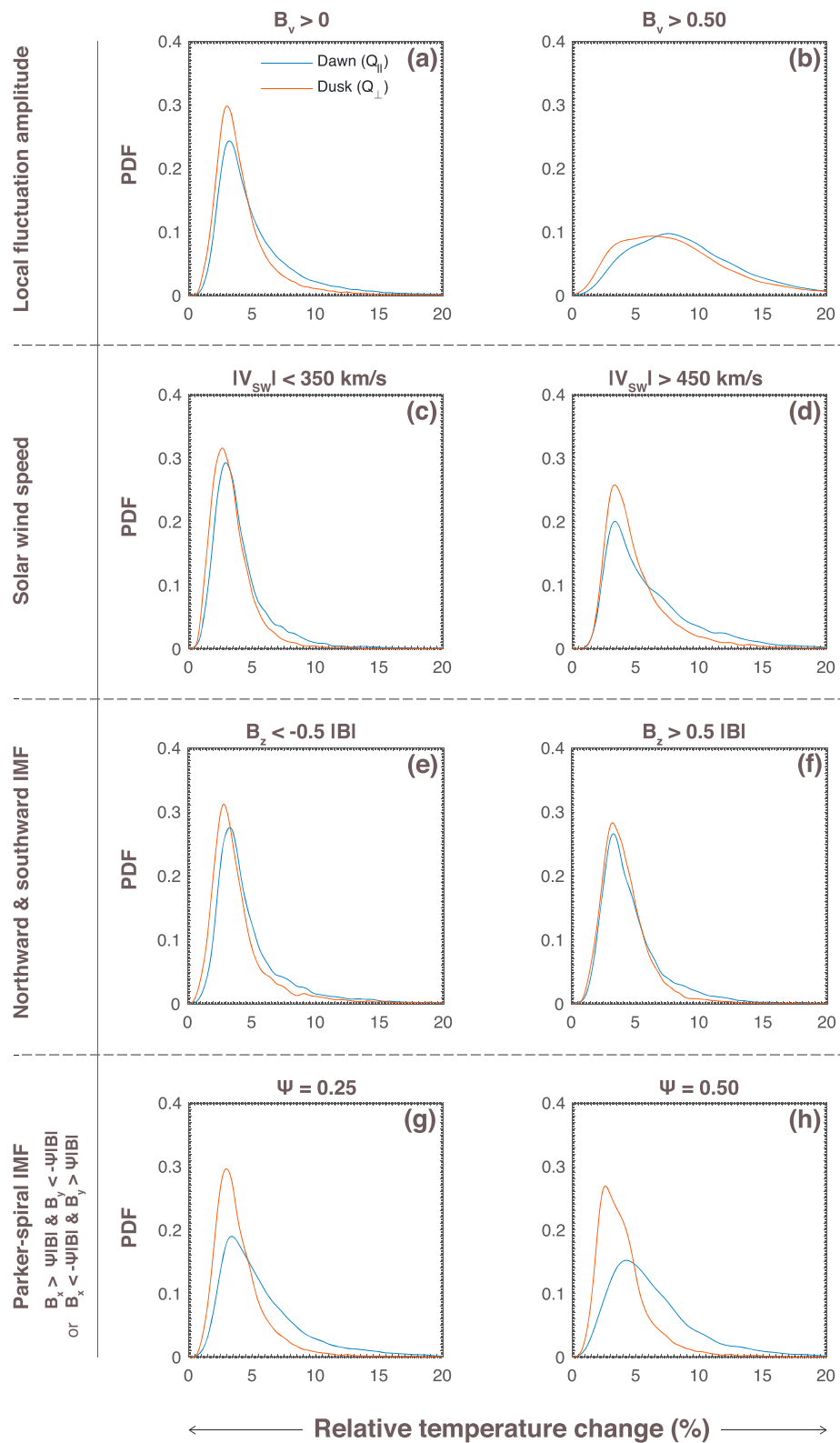


Figure 8. Probability distribution functions of T_v for the dawn (blue trace) and dusk (orange trace) flanks as a function of local and upstream conditions. (a, b) The evolution of T_v as a function of the amplitude of local ion-scale fluctuations, whereas the remaining panels show the same data but as a function of external solar wind parameters. The lower panels correspond to T_v based on the following: (c, d) solar wind speed, (e, f) northward-southward IMF, and (g, h) strength of Parker-spiral IMF.

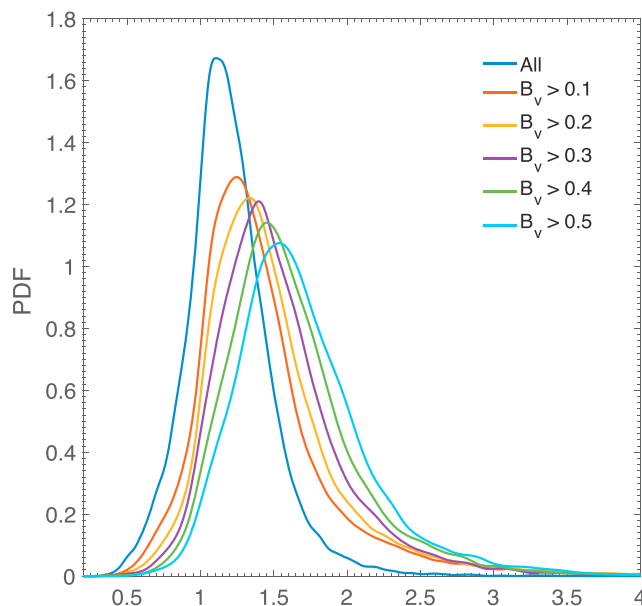


Figure 9. Probability distribution functions of the perpendicular wavelet as a function of local fluctuation amplitude B_v .

the peak is shifted from 2.5% to 3.25%, which is arguably negligible. However, the significant changes occur elsewhere: the core is substantially reduced, and more weight is shifted to the tail. In fact, the probability of $T_v > 5\%$ increases from 24% to 44% from $V_{sw} < 350$ km/s to $V_{sw} > 450$ km/s.

The statistical data of T_v as a function of B_v are plotted in Figure 7 based on cumulative subsets of T_v for $B_v > (0 : 0.1 : 0.6)$. We chose cumulative subsets as opposed to fixed bins since it is a more accurately representation of the magnetosheath; i.e., the magnetosheath turbulence is unlikely to fall in one fixed bin. The PDFs for T_v are shown in Figure 7a, whereas Figure 7b describes the change of the PDFs in Figure 7a via the change of several statistical properties (median, interquartile range, and skewness). Shown in Figure 7c are integrals of the PDFs from

Figure 7a over specific ranges. This can be interpreted as the probabilities of T_v falling within each specific range. Like the previous figure, the PDFs are distinctly non-Gaussian exhibiting a defined peak with a long tail extending past 25. By comparing the evolution of each PDF, the nature of T_v changes as a function of B_v . As the value of B_v increases, the peak decreases, and more weight is added to the tail. From $B_v > 0$ to $B_v > 0.6$ the median of T_v increases from ~ 3.8 to > 8 and the interquartile range from 2.8 to 5.5. The skewness decreased from ~ 4 to 1.6 indicating a less skewed and more Gaussian-like distribution. Interestingly, the largest change of T_v occurs in the range of $5 < T_v < 20$ as shown by comparing the blue and purple traces in Figure 7c. From $B_v > 0$ to $B_v > 0.6$ the probability of $T_v > 5$ increases from 30% to around 80%. However, there is a only a small increase of around 3% for $T_v > 20$, suggesting most of the weight is shifted in the range $5 < T_v < 20\%$. This is also suggesting that B_v has a limited and only minor impact on the extreme values of T_v . The green trace tracks the probability around the initial peak and decreases from $\sim 42\%$ to around 10%. This indicates that during high B_v , there is a diminishing probability of obtaining typical temperature variations which are most frequent during stable (low B_v) conditions. Although Figures 7b and 7c are suggestive of a linear dependency of T_v and B_v , we should state that this corresponds to distributions with different characteristics, as seen in Figure 7a. Thus, to clarify, we do not suggest that T_v increases linearly with B_v but is a manifestation of the metrics used to quantify the distribution.

To investigate the dependency on solar wind conditions and simultaneously the $Q_{||}$ - Q_{\perp} asymmetry, PDFs of T_v for the $Q_{||}$ and Q_{\perp} flanks have been plotted for multiple criteria in Figure 8. As mentioned previously, there is a $Q_{||}$ -favored asymmetry of T_v which was visible in Figure 5. In each panel (Figures 8a–8h) the $Q_{||}$ and Q_{\perp} flanks are represented by the blue and orange traces, respectively. In each panel, a $Q_{||}$ -favored asymmetry is visible; however, this differs depending on the upstream condition and magnetosheath state. In general, for high and low B_v , there is a $Q_{||}$ -favored asymmetry as seen by a shifted and “tail-heavy” distribution (Figures 8a and 8b) and appears to be enhanced during faster solar wind speed (Figures 8c and 8d). Having said that the impact on T_v is much more dramatic when binning as a function of B_v than $|V_{sw}|$ as seen by comparing Figures 8b and 8d. As concluded before, it appears that the dependency on B_v is stronger than that of T_v . During northward and southward IMF (Figures 8e and 8f), a small asymmetry is present, albeit less noticeable. Since the $Q_{||}$ - Q_{\perp} geometry in the equatorial plane is reduced when binning with northward and southward IMF, this manifests as a reduction in equatorial dawn-dusk asymmetries as seen here. To further enforce this point, we have binned the data for weakly and strongly Parker-spiral orientations (Figures 8g and 8h). The criteria for weak and strong are shown in the figure. It is immediately clear that during stronger Parker-spiral conditions, the $Q_{||}$ - Q_{\perp} asymmetry is more enhanced and the distributions become increasingly dissimilar.

This is additionally strong evidence of direct and indirect driving related to the bow shock configuration and associated processes.

Displayed in Figure 9 are PDFs of $C = B_W(\perp)/B_W(\parallel)$ for the corresponding cumulative ranges as the previous figures. According to this figure, larger C is associated with larger B_v . In turn, from the previously presented results, this implies that larger T_v is also associated with higher C . Therefore, the results presented here are composed of predominantly transverse magnetic structures.

6. Discussion

6.1. Magnetosheath Observations

The magnetosheath temperature profile regularly exhibits fluctuations (ITVs) coincident with enhanced amplitude magnetic structures at frequencies close to the proton cyclotron frequency. Our results indicate that ITVs are statistically correlated to enhancements in ion-scale magnetic field structures and appear to be driven by a variety of processes. The TH-A magnetosheath observations presented in Figures 2b–2g appear inconsistent with an electromagnetic wave and were likely caused by the transient structure recorded by TH-C upstream. On the other hand, based on the hodograms and minimum variance analysis, we identified “wave-like” structures in the MMS data (Figure 3) which exhibited an ITV smaller but comparable to those from the THEMIS case. It is noteworthy that at least two distinctly separate physical processes of comparable temporal scales manifested as in situ temperature fluctuations.

The statistical observations in Figure 4 are further confirmation that ion-scale (typically 0.2–0.4 Hz) fluctuations downstream of the Q_{\parallel} bow shock is visibly enhanced compared to its Q_{\perp} counterpart [Fairfield, 1976; Luhmann, 1986; Shevyrev *et al.*, 2007; Yao *et al.*, 2011; Chaston *et al.*, 2013; Dimmock *et al.*, 2014]. Q_{\parallel} side turbulence is understood to be driven by a plethora of mechanisms. Some of these are the following: Q_{\parallel} shock processes [Fairfield and Ness, 1970], foreshock effects [Alexandrova, 2008], solar wind fluctuations [Engebretson *et al.*, 1991], and locally generated waves and instabilities [Gary *et al.*, 1993]; the culmination of these will manifest in the measurements as a dawn-favored asymmetry as we observed. In contrast, the Q_{\perp} -magnetosheath is favored by mirror modes [Hasegawa, 1969], but these are typically 15 s [Soucek *et al.*, 2008] in duration and therefore our selection criteria would have excluded these. For this reason, the Q_{\parallel} side has a greater contribution of turbulence on shorter scales close to the ion cyclotron frequency (\sim several seconds). Quantitative analysis of our data suggested that the Q_{\parallel} -favored asymmetry of ion-scale turbulence varies depending on spatial location, but a general estimate is 35% which can increase 5–10 percentage points during faster solar wind intervals. We also observed a global increase in fluctuation amplitude during faster solar speeds of 50%–75% which occasionally exceeded 100%. This can be attributed to several factors. For example, high Mach number Q_{\parallel} shocks become nonstationary [Thomas *et al.*, 1990] and provide a source for downstream waves [Winske *et al.*, 1990]. In addition, the enhanced downstream activity [Krauss-Varban and Omid, 1991] observed during high Mach number shocks may be convected deeper into the magnetosheath proper, feeding the Q_{\parallel} side turbulence. The global increase in amplitude can be explained by the increased kinetic energy processed by the bow shock, which is redistributed into other degrees of freedom; this can manifest in the time series data as higher amplitude magnetosheath turbulence. Examples of this are mirror modes [Soucek *et al.*, 2008; Balikhin *et al.*, 2009; Génot *et al.*, 2009]. In previous studies which quantified the role of mirror mode saturation in the regulation of global magnetosheath properties, it was found that large Mach numbers resulted in high beta plasmas and saturation of mirror modes far from marginal stability [Osmane *et al.*, 2015; Dimmock *et al.*, 2015]. Although the microshock and macroshock dynamics are better left to more focused investigations, their global impact is obvious: enhanced magnetosheath turbulence and a possible source of nonadiabatic ion heating.

Elevated Q_{\parallel} side turbulence is consistent with the Q_{\parallel} side favored asymmetry of ITV amplitude shown in Figure 8. We conclude that during a typical Parker-spiral IMF orientation, the temperature profile of the Q_{\parallel} flank contains a higher occurrence of ITVs. These ITVs are coincident with enhanced amplitude magnetic structures near the in situ ion gyrofrequency, which are intrinsic to that region. This dependence is supported by Figures 5–8 which strongly suggest that enhanced ion-scale turbulence (Figure 4) drives larger ITVs.

One possible explanation for this statistical relationship is that nonadiabatic heating occurs through ion-scale structures via nonlinear wave-particle interactions. This agrees with the results reported by Chaston *et al.* [2013] and is consistent with in situ temperature changes taking place on the order of seconds. However, since we do not assess the nonadiabaticity of each event, this cannot be definitively confirmed, and we offer this

as an explanation rather than a definitive conclusion for this dependency. Nevertheless, nonadiabatic heating by ion-scale turbulence and waves is consistent with mechanisms such as that studied by *Johnson and Cheng* [2001] in which large amplitude KAWs produce stochastic particle orbits causing low energy particles (distribution core) to migrate to higher energies, producing a wider distribution. On a statistical basis, it is not feasible to study the particle distribution function in fine detail; however, ITVs are consistent with a localized widening/contraction of the distribution, which manifests as a change in the distribution second-order moment, i.e., the kinetic temperature of the population. We also estimated that pressure fluctuations ($n\delta T$) are in equipartition with ion-scale fluctuations ($\delta B^2/2\mu_0$), i.e., $\delta B^2/2\mu_0 \simeq 0.1 - 1n\delta T$.

Although KAWs (or those Doppler shifted) are known to persist throughout the magnetosheath, our results (especially the case studies in Figures 2 and 3) suggest that this process can be initiated through either waves or nonlinear structures. This effect may be enhanced when the amplitude of these variations increase, which is the case during faster solar wind speeds, as shown in Figure 6. The increase in T_v appeared stronger as a function of B_v than $|V_{sw}|$ suggesting that ITVs have a greater dependence on the small-scale magnetic fluctuations than large-scale fluid input at the shock. From a statistical standpoint, individual effects from multiple wave-particle interactions are extremely difficult to separate, and not implemented here. Having said that their combined global effects are more obvious as they could contribute to the Q_{\parallel} -favored asymmetry observed in the dayside magnetosheath [*Walsh et al.*, 2012; *Dimmock et al.*, 2015] and drive asymmetries in the magnetosphere [*Wing et al.*, 2005, 2014]. Although our data focused entirely on the magnetosheath proper, they are still relevant to the region adjacent to the magnetopause. Previous studies [*Johnson and Cheng*, 1997; *Yao et al.*, 2011] reported that KAW and ion-scale structures heat ions around the magnetopause and facilitate additional plasma transport which may reinforce the effects we have shown here.

Chaston et al. [2013] presented statistical evidence of ion heating associated with broadband ion-scale electromagnetic waves. Although their methodology differed in several aspects of this paper (they used the CGL double adiabatic model [*Chew et al.*, 1956] as a proxy for adiabatic heating), their study concluded that ion-scale magnetic field variations drive nonadiabatic heating in the magnetosheath. In our data, the probability of observing a ITV increased with the fluctuation amplitude. Similarly, *Chaston et al.* [2013] noticed an increase in the nonadiabatic invariants with the magnetic field power spectral density. Based on the statistical properties of their data set, the authors concluded that the effects in their data likely resulted from KAWs or those that had undergone Doppler shift. Our results agree with this conclusion. KAWs and similar electromagnetic waves (e.g., magnetosonic) can nonadiabatically heat ions in the magnetosheath; however, our data lead us to believe that this can also occur through other nonlinear structures [*Moore et al.*, 2016]. Based on our observations (e.g., Figure 2), we cannot attribute ITVs to a single mechanism. In both our case studies, in situ temperature changes occurred for both waves (Figure 3), and nonlinear magnetic structures (Figure 2), of which the magnetic profiles exhibited comparable temporal scale magnetic variations. *Chaston et al.* [2013] also computed the parallel and perpendicular heating rates and concluded that the broadband waves they observed were more efficient in heating in the perpendicular direction, thus increasing the temperature anisotropy. Separate analysis which we do not report also suggested that the statistical dependency was equivalent in the parallel direction, but weaker; this was not included since we could not accurately separate parallel and perpendicular heating from isotropization of the particle distribution. This introduces a complex scenario in which the magnetosheath T_{\perp}/T_{\parallel} is regulated by multiple mechanisms operating over various time scales such as mirror modes [*Soucek et al.*, 2008; *Dimmock et al.*, 2015; *Osmane et al.*, 2015], even if their interdependencies are unclear. Previous studies have suggested that such a link can be formed by a turbulent cascade [*Stasiewicz et al.*, 2001; *Bale et al.*, 2005] accounting for the energy transport from anisotropic instabilities to smaller scale kinetic structures.

Another source of magnetosheath heating is magnetic reconnection [*Retinò et al.*, 2007]. Increasing evidence [*Karimabadi et al.*, 2014] suggests that turbulence and magnetic reconnection are intrinsically related. Using a synergy of kinetic hybrid simulations and in situ data, *Karimabadi et al.* [2014] demonstrated that the bow shock is not independent of this process as it fundamentally affects the Q_{\parallel} side turbulence. Turbulent reconnection of thin current sheets on the Q_{\parallel} magnetosheath results in ion heating and subsequently contributes to the multitude of heating mechanisms already present there. It is possible (albeit difficult to confirm) that these events are present in our statistical data. The presence of turbulent reconnection in our data set could contribute to the Q_{\parallel} -favored asymmetry that was shown in Figures 5 and 8. Nevertheless, this does not alter our conclusions but strengthens our point of view. That is, Q_{\parallel} side heating is driven by a multitude of mechanisms which are influenced not only by local plasma conditions but also by external drivers.

The background, or “typical,” value of T_v is approximately $T_v = 3.1$ based on the peaks shown in Figures 6 and 7. We estimated that the statistical error per bin (σ/\sqrt{n}) for the maps shown in Figure 5 was $SE \sim 0.5$ for all conditions and $SE \sim 1$ for $B_v > 0.6$. These values should be interpreted as $T_v \pm SE$. To put this number into perspective, the increase of T_v from $B_v > 0$ to $B_v > 0.6$ is approximately 6 on the Q_{\parallel} flank; this is 4–6 times the statistical error. We would also argue that this is a conservative estimate since (1) it does not account for the changes in the PDFs shown in Figures 6–8 and (2) it is the error per bin, which is significantly smaller subsets compared to the data shown in Figures 6–8. To expand on this point, the large statistical data sets that we have collected (see Table 1) suggest that poor statistical counts should not dictate our results. In fact, the statistical error on the entire data set is negligible ($\ll 0.1$). For completeness, we also reproduced the results by scaling the B_v by the mean B_{\perp} to produce a relative wavelet amplitude. We confirm that we observe a consistent systematic relationship with T_v and that these results apply to the relative strength of the magnetic structures. Our interpretation from these calculations, validation, and the strong agreement with the existing literature is that physical processes in the data, rather than those introduced through artificial means, dictate our results.

6.2. Global Impact

The cold component ions in the cold dense plasma sheet are estimated to be hotter on the dawnside by approximately 40% [Wing *et al.*, 2005, 2014] compared to the dusk. This is partially explained by the 15–20% Q_{\parallel} -favored asymmetry of magnetosheath ion temperatures [Walsh *et al.*, 2012; Dimmock *et al.*, 2015], but still, open questions remain on what could account for this gap. The aforementioned studies focused on the seed temperature averaged over several minutes; however, the contributions from the effects shown here may have been excluded from these results. It has been demonstrated thorough kinetic hybrid simulations [Karimabadi *et al.*, 2014] that kinetic processes inherent to the Q_{\parallel} magnetosheath can dictate their global properties. The combination of seed temperatures, fast saturation of mirror mode structures, and the contribution of the transient effects could partly explain the difference of asymmetry values between the magnetosheath and cold dense plasma sheet. Although we have excluded data close to the magnetopause, it has been shown that similar magnetic field structures in this region can facilitate additional plasma transport [Yao *et al.*, 2011]. This is evidenced by work performed by a number of authors [Johnson and Cheng, 2001; Johnson *et al.*, 2001; Chaston *et al.*, 2008] who reported that ion heating through wave-particle interactions at the magnetopause can act as a diffusive plasma transport mechanism. Therefore, the global magnetospheric impact from magnetosheath plasma properties is a function of both its steady (fluid) and transient (kinetic) states. Understanding the cross-scale coupling between kinetic and fluid-scale processes [Moore *et al.*, 2016] will be fundamental not only to magnetospheric physics but is a fundamental physical problem.

7. Conclusions and Summary

The main results from this manuscript can be summarized as follows:

1. In situ temperature fluctuations were observed in the dayside magnetosheath directly coinciding with enhancements in ion-scale magnetic field structures
2. Temperature variations are not limited to one mechanism but can be induced by wave packets (e.g., kinetic Alfvén waves) or localized nonlinear structures of external driving (e.g., IMF discontinuities)
3. Our data suggested a Q_{\parallel} - Q_{\perp} asymmetry. There is larger probability of higher amplitude temperature changes on the Q_{\parallel} magnetosheath for similar conditions. This is indicative that shock-related turbulence/processes or foreshock transients may play a role.
4. A statistical study by THEMIS suggested that larger amplitude magnetic field variations induce larger relative changes in temperature.
5. Results are consistent with previous studies [Chaston *et al.*, 2008; Yao *et al.*, 2011; Chaston *et al.*, 2013] reporting that ion-scale waves such as kinetic Alfvén waves result in nonadiabatic temperature increases.
6. Larger temperature variations were observed for higher amplitude structures as opposed to fast solar wind; i.e., the local kinetic effects are stronger than the fluid input at the shock.
7. The kinetic effects shown here may contribute to the existing magnetosheath Q_{\parallel} temperature asymmetry and could shed further light on the 40% asymmetry of cold component ions in the cold dense plasma sheet.

To summarize, we have presented observations of magnetosheath in situ ion temperature changes coinciding with ion-scale magnetic field structures. The results from this paper are a clear demonstration that the magnetosheath is a complex dynamical system and that plasma processes are intrinsically related. This is being recognized by the increasing complexity of (and drive for) global and local kinetic simulations

[Karimabadi et al., 2014; Omidi et al., 2014; Palmroth et al., 2015], which aim to accurately model the behavior of the dynamic magnetosheath. More specifically, the ability for codes to reproduce the non-Gaussian distributions of plasma properties shown here and other studies. This is essential in moving forward in developing a more complete understand of the processes inherent to solar wind magnetosheath coupling. For dawn-dusk asymmetries, it is vital to consider both the underlying seed asymmetries and those which are more transient in nature as shown here. Future work should focus on determining the global impact from such events and incorporating this complex behavior into existing models. In addition, these results may also be applicable to other plasma parameters such as density and velocity. Evidence of this can be found in the two case studies in the sense that density and velocity also appeared affected by the magnetic structures. Although worth investigating, it is beyond the scope of the present study. Finally, this analysis could be extended to electron scales using higher cadence (burst) data from MMS.

Acknowledgments

A. P. Dimmock was funded by the Academy of Finland grant 288472. T. I. Pulkkinen and A. Osmane were supported by the Academy of Finland grants 267073/2013 and 297688/2015, respectively. E. Kilpua acknowledges the Academy of Finland project 1218152. K. Nykyri was supported by the NASA grant NNX16AF89G, and the NSF grant 1502774. We acknowledge use of NASA/GSFC's Space Physics Data Facility's OMNIWeb (<http://omniweb.gsfc.nasa.gov>) service, and OMNI data. Authors would also like to thank the THEMIS instrument teams for the use of their data. The THEMIS data are accessed via <http://themis.ssl.berkeley.edu/index.shtml> free of charge. We would also like to acknowledge the MMS team, especially the FGM and FPI instrument teams. All MMS data were downloaded through the MMS Science Data Center accessible at <https://lasp.colorado.edu/mms/sdc/public/>, and we recognize the efforts from all who contribute to this service.

References

- Alexandrova, O. (2008), Solar wind vs magnetosheath turbulence and Alfvén vortices, *Nonlinear Processes Geophys.*, *15*, 95–108.
- Angelopoulos, V. (2008), The THEMIS mission, *Space Sci. Rev.*, *141*, 5–34, doi:10.1007/s11214-008-9336-1.
- Auster, H. U., et al. (2008), The THEMIS Fluxgate Magnetometer, *Space Sci. Rev.*, *141*, 235–264, doi:10.1007/s11214-008-9365-9.
- Bale, S. D., P. J. Kellogg, F. S. Mozer, T. S. Horbury, and H. Reme (2005), Measurement of the electric fluctuation spectrum of magnetohydrodynamic turbulence, *Phys. Rev. Lett.*, *94*, 215002, doi:10.1103/PhysRevLett.94.215002.
- Balikhin, M. A., R. Z. Sagdeev, S. N. Walker, O. A. Pokhotelov, D. G. Sibeck, N. Beloff, and G. Dudnikova (2009), THEMIS observations of mirror structures: Magnetic holes and instability threshold, *Geophys. Res. Lett.*, *36*, L03105, doi:10.1029/2008GL036923.
- Biskamp, D., and H. Welter (1972), Numerical studies of magnetosonic collisionless shock waves, *Nuclear Fusion*, *12*, 663, doi:10.1088/0029-5515/12/6/006.
- Blanco-Cano, X., N. Omidi, and C. T. Russell (2006), Macrostructure of collisionless bow shocks: 2. ULF waves in the foreshock and magnetosheath, *J. Geophys. Res.*, *111*, A10205, doi:10.1029/2005JA011421.
- Borovsky, J. E., M. Hesse, J. Birn, and M. M. Kuznetsova (2008), What determines the reconnection rate at the dayside magnetosphere?, *J. Geophys. Res.*, *113*, A07210, doi:10.1029/2007JA012645.
- Burch, J. L., T. E. Moore, R. B. Torbert, and B. L. Giles (2016), Magnetospheric multiscale overview and science objectives, *Space Sci. Rev.*, *199*(1), 5–21, doi:10.1007/s11214-015-0164-9.
- Chaston, C., et al. (2008), Turbulent heating and cross-field transport near the magnetopause from THEMIS, *Geophys. Res. Lett.*, *35*, L17508, doi:10.1029/2008GL033601.
- Chaston, C. C., Y. Yao, N. Lin, C. Salem, and G. Ueno (2013), Ion heating by broadband electromagnetic waves in the magnetosheath and across the magnetopause, *J. Geophys. Res. Space Physics*, *118*, 5579–5591, doi:10.1002/jgra.50506.
- Chew, G. F., M. L. Goldberger, and F. E. Low (1956), The Boltzmann equation and the one-fluid hydromagnetic equations in the absence of particle collisions, *Proc. R. Soc. London, Ser. A*, *236*, 112–118, doi:10.1098/rspa.1956.0116.
- Dimmock, A. P., and K. Nykyri (2013), The statistical mapping of magnetosheath plasma properties based on THEMIS measurements in the magnetosheath interplanetary medium reference frame, *J. Geophys. Res. Space Physics*, *118*, 4963–4976, doi:10.1002/jgra.50465.
- Dimmock, A. P., M. A. Balikhin, S. N. Walker, and S. A. Pope (2013), Dispersion of low frequency plasma waves upstream of the quasi-perpendicular terrestrial bow shock, *Ann. Geophys.*, *31*, 1387–1395, doi:10.5194/angeo-31-1387-2013.
- Dimmock, A. P., K. Nykyri, and T. I. Pulkkinen (2014), A statistical study of magnetic field fluctuations in the dayside magnetosheath and their dependence on upstream solar wind conditions, *J. Geophys. Res. Space Physics*, *119*, 6231–6248, doi:10.1002/2014JA020009.
- Dimmock, A. P., K. Nykyri, H. Karimabadi, A. Osmane, and T. I. Pulkkinen (2015), A statistical study into the spatial distribution and dawn-dusk asymmetry of dayside magnetosheath ion temperatures as a function of upstream solar wind conditions, *J. Geophys. Res. Space Physics*, *120*, 2767–2782, doi:10.1002/2014JA020734.
- Dungey, J. W. (1961), Interplanetary magnetic field and the auroral zones, *Phys. Rev. Lett.*, *6*, 47–48.
- Eastwood, J. P., A. Balogh, M. W. Dunlop, T. S. Horbury, and I. Dandouras (2002), Cluster observations of fast magnetosonic waves in the terrestrial foreshock, *Geophys. Res. Lett.*, *29*(22), 2046, doi:10.1029/2002GL015582.
- Engebretson, M. J., N. Lin, W. Baumjohann, H. Luehr, and B. J. Anderson (1991), A comparison of ULF fluctuations in the solar wind, magnetosheath, and dayside magnetosphere. I—Magnetosheath morphology. II—Field and plasma conditions in the magnetosheath, *J. Geophys. Res.*, *96*, 3441–3464, doi:10.1029/90JA02101.
- Fairfield, D. H. (1976), Magnetic fields of the magnetosheath, *Rev. Geophys. Space Phys.*, *14*, 117–134, doi:10.1029/RG014i001p00117.
- Fairfield, D. H., and N. F. Ness (1970), Magnetic field fluctuations in the Earth's magnetosheath, *J. Geophys. Res.*, *75*, 6050, doi:10.1029/JA075i031p06050.
- Farris, M. H., and C. T. Russell (1994), Determining the standoff distance of the bow shock: Mach number dependence and use of models, *J. Geophys. Res.*, *99*, 17,681–17,689, doi:10.1029/94JA01020.
- Gary, S. P., S. A. Fuselier, and B. J. Anderson (1993), Ion anisotropy instabilities in the magnetosheath, *J. Geophys. Res.*, *98*, 1481–1488, doi:10.1029/92JA01844.
- Génot, V., E. Budnik, P. Hellinger, T. Passot, G. Belmont, P. M. Trávníček, P.-L. Sulem, E. Lucek, and I. Dandouras (2009), Mirror structures above and below the linear instability threshold: Cluster observations, fluid model and hybrid simulations, *Ann. Geophys.*, *27*, 601–615, doi:10.5194/angeo-27-601-2009.
- Gutynska, O., D. G. Sibeck, and N. Omidi (2015), Magnetosheath plasma structures and their relation to foreshock processes, *J. Geophys. Res. Space Physics*, *120*, 7687–7697, doi:10.1002/2014JA020880.
- Hasegawa, A. (1969), Drift mirror instability of the magnetosphere, *Phys. Fluids*, *12*, 2642–2650, doi:10.1063/1.1692407.
- Johnson, J. R., and C. Z. Cheng (1997), Kinetic Alfvén waves and plasma transport at the magnetopause, *Geophys. Res. Lett.*, *24*, 1423–1426, doi:10.1029/97GL01333.
- Johnson, J. R., and C. Z. Cheng (2001), Stochastic ion heating at the magnetopause due to kinetic Alfvén waves, *Geophys. Res. Lett.*, *28*, 4421–4424, doi:10.1029/2001GL013509.
- Johnson, J. R., and S. Wing (2009), Northward interplanetary magnetic field plasma sheet entropies, *J. Geophys. Res.*, *114*, A00D08, doi:10.1029/2008JA014017.

- Johnson, J. R., C. Z. Cheng, and P. Song (2001), Signatures of mode conversion and kinetic alfvén waves at the magnetopause, *Geophys. Res. Lett.*, *28*(2), 227–230, doi:10.1029/2000GL012048.
- Karimabadi, H., et al. (2014), The link between shocks, turbulence, and magnetic reconnection in collisionless plasmas, *Phys. Plasmas*, *21*(6), 062308, doi:10.1063/1.4882875.
- King, J. H., and N. E. Papitashvili (2005), Solar wind spatial scales in and comparisons of hourly Wind and ACE plasma and magnetic field data, *J. Geophys. Res.*, *110*, A02104, doi:10.1029/2004JA010649.
- Krauss-Varban, D., and N. Omid (1991), Structure of medium Mach number quasi-parallel shocks—Upstream and downstream waves, *J. Geophys. Res.*, *96*, 17,715–17,731, doi:10.1029/91JA01545.
- Lavraud, B., et al. (2013), Asymmetry of magnetosheath flows and magnetopause shape during low Alfvén Mach number solar wind, *J. Geophys. Res. Space Physics*, *118*, 1089–1100, doi:10.1002/jgra.50145.
- Lee, L. C., C. S. Wu, and X. W. Hu (1986), Increase of ion kinetic temperature across a collisionless shock. I—A new mechanism, *Geophys. Res. Lett.*, *13*, 209–212, doi:10.1029/GL013i003p00209.
- Lee, L. C., M. E. Mandt, and C. S. Wu (1987), Increase of ion kinetic temperature across a collisionless shock. II—A simulation study, *J. Geophys. Res.*, *92*, 13,438–13,446, doi:10.1029/JA092iA12p13438.
- Longmore, M., S. J. Schwartz, J. Geach, B. M. A. Cooling, I. Dandouras, E. A. Lucek, and A. N. Fazakerley (2005), Dawn-dusk asymmetries and sub-Alfvénic flow in the high and low latitude magnetosheath, *Ann. Geophys.*, *23*, 3351–3364, doi:10.5194/angeo-23-3351-2005.
- Luhmann, J. G. (1986), The solar wind interaction with Venus, *Space Sci. Rev.*, *44*, 241–306, doi:10.1007/BF00200818.
- McFadden, J. P., C. W. Carlson, D. Larson, M. Ludlam, R. Abiad, B. Elliott, P. Turin, M. Marckwordt, and V. Angelopoulos (2008), The THEMIS ESA plasma instrument and in-flight calibration, *Space Sci. Rev.*, *141*, 277–302, doi:10.1007/s11214-008-9440-2.
- Miura, A., and P. L. Pritchett (1982), Nonlocal stability analysis of the MHD Kelvin-Helmholtz instability in a compressible plasma, *J. Geophys. Res.*, *87*(A9), 7431–7444, doi:10.1029/JA087iA09p07431.
- Moore, T. W., K. Nykyri, and A. P. Dimmock (2016), Cross-scale energy transport in space plasmas, *Nat. Phys.*, *12*, 1164–1169.
- Němeček, Z., M. Hayosh, J. Safránková, G. N. Zastenker, and J. D. Richardson (2003), The dawn-dusk asymmetry of the magnetosheath: INTERBALL-1 observations, *Adv. Space Res.*, *31*, 1333–1340, doi:10.1016/S0273-1177(03)00007-3.
- Nykyri, K., and A. Otto (2001), Plasma transport at the magnetospheric boundary due to reconnection in Kelvin-Helmholtz vortices, *Geophys. Res. Lett.*, *28*(18), 3565–3568.
- Omid, N., H. Zhang, C. Chu, D. Sibeck, and D. Turner (2014), Parametric dependencies of spontaneous hot flow anomalies, *J. Geophys. Res. Space Physics*, *119*(12), 9823–9833, doi:10.1002/2014JA020382.
- Osmane, A., A. P. Dimmock, and T. I. Pulkkinen (2015), Universal properties of mirror mode turbulence in the Earth's magnetosheath, *Geophys. Res. Lett.*, *42*, 3085–3092, doi:10.1002/2015GL063771.
- Palmroth, M., M. Archer, R. Vainio, H. Hietala, Y. Pfau-Kempf, S. Hoilijoki, O. Hannuksela, U. Ganse, A. Sandroos, S. V. Alfthan, and J. P. Eastwood (2015), ULF foreshock under radial IMF: THEMIS observations and global kinetic simulation Vlasiator results compared, *J. Geophys. Res. Space Physics*, *120*, 8782–8798, doi:10.1002/2015JA021526.
- Paularena, K. I., J. D. Richardson, M. A. Kolpak, C. R. Jackson, and G. L. Siscoe (2001), A dawn-dusk density asymmetry in Earth's magnetosheath, *J. Geophys. Res.*, *106*, 25,377–25,394, doi:10.1029/2000JA000177.
- Pollock, C., et al. (2016), Fast plasma investigation for magnetospheric multiscale, *Space Sci. Rev.*, *199*(1), 331–406, doi:10.1007/s11214-016-0245-4.
- Retinò, A., D. Sundkvist, A. Vaivads, F. Mozer, M. André, and C. J. Owen (2007), In situ evidence of magnetic reconnection in turbulent plasma, *Nat. Phys.*, *3*, 236–238, doi:10.1038/nphys574.
- Russell, C. T., et al. (2016), The magnetospheric multiscale magnetometers, *Space Sci. Rev.*, *199*(1), 189–256, doi:10.1007/s11214-014-0057-3.
- Shevryev, N. N., G. N. Zastenker, and J. Du (2007), Statistics of low-frequency variations in solar wind, foreshock and magnetosheath: INTERBALL-1 and CLUSTER data, *Planet. Space Sci.*, *55*, 2330–2335, doi:10.1016/j.pss.2007.05.014.
- Shue, J.-H., et al. (1998), Magnetopause location under extreme solar wind conditions, *J. Geophys. Res.*, *103*, 17,691–17,700, doi:10.1029/98JA01103.
- Sonnerup, B. U. O., and L. J. Cahill Jr. (1967), Magnetopause structure and attitude from Explorer 12 observations, *J. Geophys. Res.*, *72*, 171–183, doi:10.1029/JZ072i001p00171.
- Soucek, J., E. Lucek, and I. Dandouras (2008), Properties of magnetosheath mirror modes observed by Cluster and their response to changes in plasma parameters, *J. Geophys. Res.*, *113*, A04203, doi:10.1029/2007JA012649.
- Stasiewicz, K., C. E. Seyler, F. S. Mozer, G. Gustafsson, J. Pickett, and B. Popielawska (2001), Magnetic bubbles and kinetic Alfvén waves in the high-latitude magnetopause boundary, *J. Geophys. Res.*, *106*(A12), 29,503–29,514, doi:10.1029/2001JA900055.
- Thomas, V. A., D. Winske, and N. Omid (1990), Re-forming supercritical quasi-parallel shocks. I—One- and two-dimensional simulations, *J. Geophys. Res.*, *95*, 18,809–18,819, doi:10.1029/JA095iA11p18809.
- Verigin, M., J. Slavin, A. Szabo, G. Kotova, and T. Gombosi (2003), Planetary bow shocks: Asymptotic MHD Mach cones, *Earth Planets Space*, *55*, 33–38.
- Verigin, M. I., et al. (2001), Analysis of the 3-D shape of the terrestrial bow shock by INTERBALL/MAGION 4 observations, *Adv. Space Res.*, *28*, 857–862, doi:10.1016/S0273-1177(01)00502-6.
- Verigin, M. I., M. Tátrallyay, G. Erdős, and G. A. Kotova (2006), Magnetosheath interplanetary medium reference frame: Application for a statistical study of mirror type waves in the terrestrial plasma environment, *Adv. Space Res.*, *37*, 515–521, doi:10.1016/j.asr.2005.03.042.
- Walsh, B. M., D. G. Sibeck, Y. Wang, and D. H. Fairfield (2012), Dawn-dusk asymmetries in the Earth's magnetosheath, *J. Geophys. Res.*, *117*, A12211, doi:10.1029/2012JA018240.
- Wing, S., J. R. Johnson, P. T. Newell, and C.-I. Meng (2005), Dawn-dusk asymmetries, ion spectra, and sources in the northward interplanetary magnetic field plasma sheet, *J. Geophys. Res.*, *110*, A08205, doi:10.1029/2005JA011086.
- Wing, S., et al. (2014), Review of solar wind entry into and transport within the plasma sheet, *Space Sci. Rev.*, *184*(1–4), 33–86, doi:10.1007/s11214-014-0108-9.
- Winske, D., V. A. Thomas, N. Omid, and K. B. Quest (1990), Re-forming supercritical quasi-parallel shocks. II—Mechanism for wave generation and front re-formation, *J. Geophys. Res.*, *95*, 18,821–18,832, doi:10.1029/JA095iA11p18821.
- Yao, Y., C. C. Chaston, K.-H. Glassmeier, and V. Angelopoulos (2011), Electromagnetic waves on ion gyro-radii scales across the magnetopause, *Geophys. Res. Lett.*, *38*, L09102, doi:10.1029/2011GL047328.